



Modeling and optimization of galvanometric point-scanning temporal dynamics

ERIC M. TANG  AND YUANKAI K. TAO*

Vanderbilt University, Department of Biomedical Engineering, Nashville, Tennessee 37232, USA

*yuankai.tao@vanderbilt.edu

Abstract: Galvanometers are ubiquitous in point-scanning applications in optical imaging, display, ranging, manufacturing, and therapeutic technologies. However, galvanometer performance is constrained by finite response times related to mirror size and material properties. We present a model-driven approach for optimizing galvanometer response characteristics by tuning the parameters of the closed-loop galvanometer controller and demonstrate settling time reduction by over 50%. As an imaging proof-of-concept, we implement scan waveforms that take advantage of the optimized galvanometer frequency response to increase linear field-of-view, signal-to-noise ratio, contrast-to-noise ratio, and speed. The hardware methods presented may be directly implemented on galvanometer controllers without the need for specialized equipment and used in conjunction with customized scan waveforms to further optimize scanning performance.

© 2021 Optical Society of America under the terms of the [OSA Open Access Publishing Agreement](#)

1. Introduction

Scanning technologies are integral to a broad range of optics applications including microscopy [1–4], ophthalmoscopy [5–8], optical coherence tomography (OCT) [9], optical ranging (LIDAR) [10], and prototyping and manufacturing [11–14]. The most commonly used scanning technologies can be divided into four categories: resonant scanners, polygon scanners, acousto-optic deflectors (AODs), and galvanometer scanners. The temporal response of these devices is bandlimited and the corresponding finite settling time of the scanner fundamentally limits performance parameters such as scanning speed, linearity, trajectory, field-of-view (FOV), and/or resolution.

1.1. Resonant scanners

Resonant scanners have high scanning speeds (> 10 kHz line rate) and low power consumption, making them ideal for microscopy [15–17], OCT [18], light-sheet imaging [19], and adaptive optics [6,20–22]. Compact form-factor microelectromechanical system (MEMS) resonant scanners are also often used in displays and laser scanning systems [23,24]. However, resonant scanners are limited in their ability to randomly target regions-of-interest (ROIs) because they must be driven with sinusoidal waveforms close to their resonant frequency. While the amplitude of the resonant scan waveform can be modulated, sampling along the sinusoidal scan trajectory is necessarily nonlinear and requires additional calibration, nonlinear analog-to-digital converter (ADC) sampling, or post-processing to relinearize the acquired images [25–27]. Nonlinear scanning also results in nonuniform illumination/optical power deposition across samples, which contribute to increased tissue damage and photobleaching at the edges of the FOV where dwell time is increased in fluorescence applications. Acousto-optic and electro-optic modulators can be used to modulate laser intensity across the field, but these methods significantly increase system cost and complexity [28].

1.2. Polygon scanners

Polygon scanners combine a high-speed motor with multiple mirror facets to achieve > 100 kHz line rates [29–34]. The lack of oscillatory elements enables constant linear velocity scanning over large FOVs. However, the facet size and rotation speed of polygon mirrors are fixed and, thus, also fix the FOV and minimum ADC sampling requirements. In addition, all detection electronics are generally required to be synchronized off of the polygon clock. Manufacturing and assembly of polygon mirror facets can also introduce defects that result in facet-to-facet angle variance, facet radii variance, surface nonuniformity, and surface reflectance differences [35]. Polygon mirror scan angles are directly proportional to the number of facets, thus, requiring custom-designed scan optics to match specific mirror geometries. The size of polygon mirrors is also proportional to the aperture size and number of facets, which generally precludes applications in space constrained devices, such as compact handheld devices. Applications that require descanning or two-dimensional scanning will also require complex system geometries and additional scanning/translational elements.

1.3. Acousto-optic deflectors

Acousto-optic deflectors (AODs) are primarily used in applications requiring extremely high-speed scanning (> 1 MHz line rate) or randomly addressable scan trajectories because they do not require mechanical elements [36–38]. However, the diffraction angle of AODs is wavelength-dependent and induces chromatic dispersion that is coupled with group velocity dispersion induced by the AOD. AODs also suffer from significantly lower power throughput compared to reflective scanners (60% vs. $>90\%$ optical efficiency) due to both material dispersion and loss to multiple diffraction orders [39]. Spatial and temporal broadening requires precompensation using prism pairs or diffraction gratings, which increase system cost, complexity, and optical loss [40]. Furthermore, the small aperture of these devices limits the maximum deflection angle and number of resolvable spots, thereby reducing the FOV and spatial resolution of the system. The wavelength-dependent deflection of AODs also prevents its use in systems that require descanning, such as in fluorescence imaging.

1.4. Galvanometer scanners

Galvanometers are the most commonly used scanners for biomedical imaging [41–44] due to their moderate speed (> 1 kHz), low step response times (~ 100 μ s for 3 mm apertures), and high positional accuracy [45]. Additionally, closed-loop controller feedback of mirror position can be used to optimize galvanometer inputs to improve linearity and minimize positional errors. Compared to resonant scanners, closed-loop galvanometers enable imaging of a large FOV with high linearity and adjustable speed. Galvanometers also do not suffer from facet-to-facet variability as compared to polygon mirrors or high loss and dispersive effects as compared to AODs. In addition, galvanometer pairs can be used to randomly address scan trajectories to target ROIs.

Despite the aforementioned advantages of galvanometers, their performance is directly related to response time optimizations specific to mirror size, material stiffness, weight, and alignment [45]. Previously demonstrated methods for scanner optimization include iterative learning control [46,47], Landweber-based deconvolution [48], and optimization of input scan waveform shape, frequency, and amplitude [49–51]. However, these methods are dependent on a specific input scan waveform and are not robustly suitable for imaging applications that require changing the FOV, speed, or sampling density of the scan. Here, we take advantage of the closed-loop feedback of proportional-integral-derivative (PID) controllers to optimize the response of galvanometer scanners to arbitrary input waveforms. By modifying fundamental PID parameters (e.g., error proportional gain and low and high frequency damping gains), it is possible to significantly improve galvanometer controller frequency response and reduce settling time [52–54]. We show

that we can halve galvanometer response time to enable high speed imaging of dynamics and increased scanning FOV, which can have broad-ranging benefits in object detection, ranging, and tracking as well as other scanning applications. As a proof-of-concept, we perform functional ophthalmic imaging using optical coherence tomographic angiography (OCTA) [55], and propose several software optimization methods that leverage optimized galvanometer response times to further improve imaging performance.

2. Methods

2.1. Experimental setup

Small (X) and large (Y) galvanometer mirrors with 5 mm pupil diameters (Saturn 5B, ScannerMax – Supplement 1 Fig. 1) were interfaced with a custom 400 kHz swept-source OCT engine [56,57]. Image acquisition and galvanometer scanning were synchronized using an external laser line trigger and data acquisition device (USB-6351, National Instruments). A field-programmable gated array (cRIO-9053, National Instruments) was used to stream X and Y-mirror positions from the analog output channels of the galvanometer PID controller (MachDSP, ScannerMax) (Fig. 1(a)).

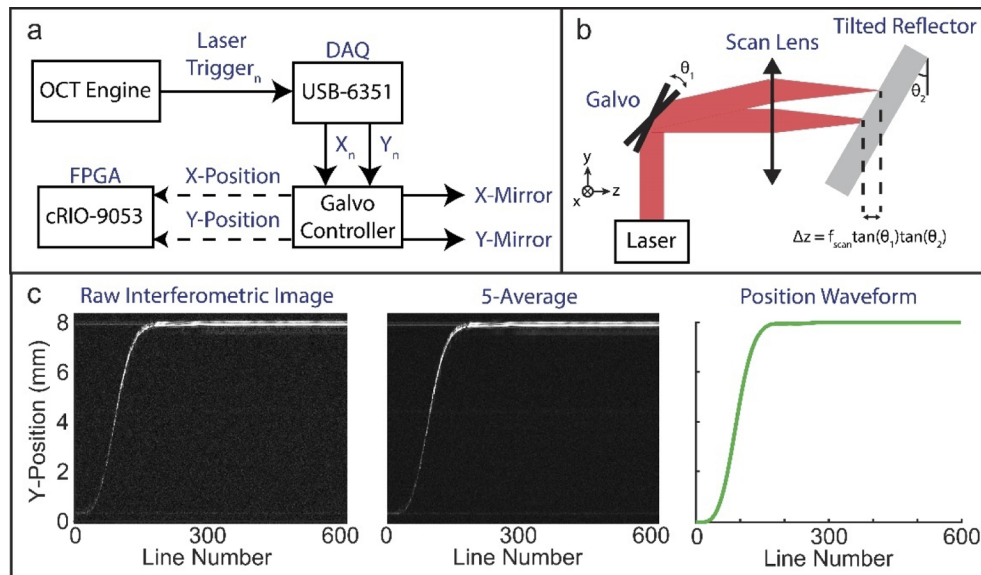


Fig. 1. Measurements of galvanometer step response. (a) Experimental setup. A DAQ device generates X- and Y-mirror position outputs for each laser line trigger. The galvanometer controller processes the input signals and outputs them to the mirrors. A FPGA simultaneously measures the mirror positions directly from the controller. (b) Simplified diagram depicting imaging of the tilted reflector, which enables sampling of galvanometer position as a function of depth. (c) Processing and extraction of position waveforms from optical measurements.

2.2. Optimization criteria

Closed-loop feedback of the galvanometer controller facilitated hardware optimization by providing access to basic tuning parameters (error proportional servo gain, low and high frequency damping gain, position error integral gain, and position proportional gain) and several intermediate tuning parameters (Supplement 1 Fig. 2). For optimization, a settling time criteria was chosen as it provides a quantitative metric describing the performance of the PID controller

for different tuning parameter values and is a direct reflection of the frequency response of the system [58]. Here, the time that the mirror took to settle to its final position within an error band after a step response was denoted as the total settling time. In this imaging demonstration, this error band was set to the lateral resolution limit of the imaging system ($11.1\ \mu\text{m}$) since oscillations below the resolution limit cannot be resolved.

Galvanometer step responses and corresponding settling times were measured electronically using mirror positional outputs from the galvanometer PID controller (Fig. 1 (a)). PID positional outputs were validated against optical interferometry measurements made by imaging a tilted reflector with a flat scattering surface (Fig. 1(b) and (c)). Interferometric measurements allowed remapping of lateral galvanometer scan positions to axial displacements scaled by the tangent of the tilt angle, which effectively enables measurement of galvanometer angular position with arbitrary accuracy up to the image signal-to-noise (SNR) limit (Fig. 1(b)). This allowed for significantly higher spatial resolution than would otherwise be possible using standard test-chart measurements, which are sampling-limited by the convolution of imaging spot size and test-chart feature size.

The Y-mirror settling time for different input step function amplitudes and manufacturer provided PID tuning parameters were measured both electronically and optically (Fig. 2 and Supplement 1 Table 1). Manufacturer PID tunings were designed to have high position accuracy (Tuning 1), high position accuracy and bandwidth for stable scanning at high speeds (Tuning 2), and high bandwidth (Tuning 3). A total of 100 electronic and optical measurements were acquired for each tuning and step amplitude combination. Tilted reflector depth profiles were 5-averaged to reduce noise and measurement variability, and position waveforms were referenced to the axial intensity peak. Electronic and optical measurements of settling times and positions were

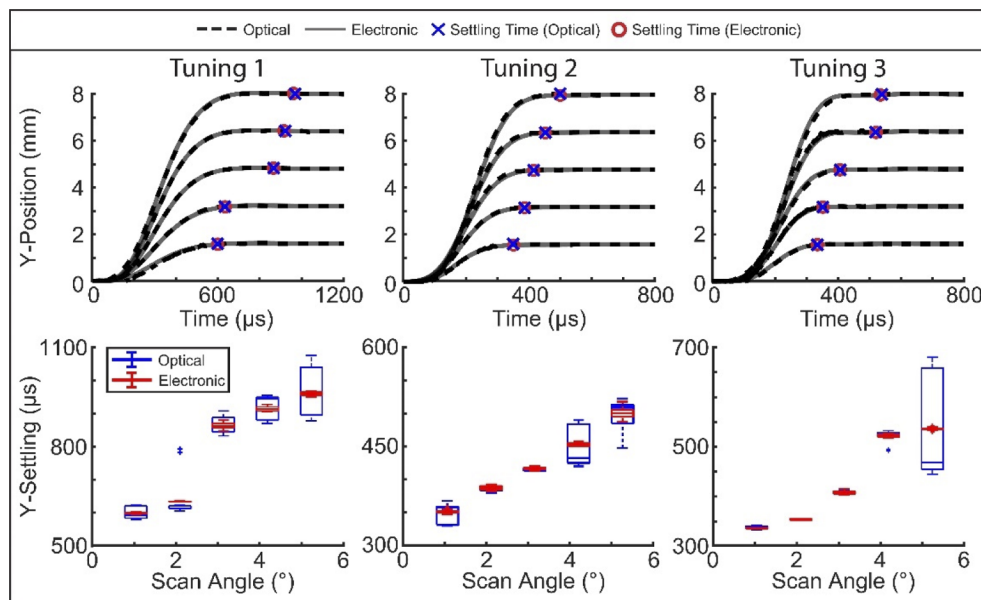


Fig. 2. Comparison of electronically and optically measured galvanometer step response. Top row: Optically (dashed) and electronically (solid) measured Y-mirror step response and settling times (crosses and circles) for three manufacturer provided tunings at input step function amplitudes 1.6 mm, 3.2 mm, 4.8 mm, 6.4 mm, and 8 mm. Bottom row: Settling times for each tuning at different step amplitudes show no statistical differences between optical and electronic measurements ($p > 0.05$, $n=100$).

equivalent (Fig. 2, top row) and statistical analysis showed no significant difference ($p > 0.05$) between the methods (Fig. 2, bottom row). Large standard deviations in the optical measurements are from underdamped responses caused by ringing of the mirror during settling that was likely filtered by the PID controller onboard electronics and not present in the corresponding electronic measurements. This was not a limitation of the electronic measurements, because the mean settling time in underdamped cases were consistently higher than critical damping cases and subsequently removed from the galvanometer optimization search space. Given this validation data, all subsequent measurements were made electronically, which obviated the need for image post-processing, showed significantly decreased measurement variability related to spatial differences in scattering across the tilted reflector, and may be directly implemented without specialized test equipment.

2.3. Gaussian process regression

Galvanometer optimization was performed by iteratively modifying PID tuning parameters using manufacturer-provided controller software to minimize step response settling time. First, a sparse sweep of the 5 basic parameters (error proportional servo gain, low and high frequency damping gains, position error integral gain, position proportional gain) was performed. Each parameter was incremented by a step size of 100 over a full range of 0-1000. Figure 3 shows an example of a single optimization iteration for 2 parameters. For each set of parameters, a position waveform was measured and the corresponding settling time was calculated as the time from the step start to when the position waveform settled to within a lateral full-width at half-maximum (FWHM) spot size ($11.1 \mu\text{m}$) of the final steady-state position (Fig. 3(a)). Parameter values that caused the scanner to be unresponsive were excluded, resulting in a total of 10,602 unique basic parameter configurations (N_1).

A Gaussian process regression (GPR) model of settling time values was created (MATLAB, MathWorks) to narrow down the range of optimal basic parameter values over the complex nonlinear parameter space. GPR is a nonparametric, Bayesian regression method with significant performance advantages over conventional linear regression models [59,60]. In general, a Gaussian process is defined as a multivariate Gaussian distribution where each observation acts as a random variable. Thus, for N given data points or observations, the corresponding Gaussian process would be N -dimensional. As a result, each data point has an associated mean and covariance describing the probability distribution of values for that specific input. GPR modeling begins with an assumed prior distribution that will be updated given a set of observations:

$$S_0 \sim \mathcal{N}(\mu_0, K(X_0, X_0)) \quad (1)$$

Here, the prior settling time distribution, S_0 , is defined as a joint Gaussian distribution with a mean of $\mu_0 = 0$ and a covariance matrix $K(X_0, X_0)$, where:

$$K(X_0, X_0) = \begin{bmatrix} k(x_0^1, x_0^1) & \cdots & k(x_0^1, x_0^N) \\ \vdots & \ddots & \vdots \\ k(x_0^N, x_0^1) & \cdots & k(x_0^N, x_0^N) \end{bmatrix} \quad (2)$$

The covariance matrix, K , is created by evaluating a covariance kernel function k for each combination of inputs X_0 that span the parameter tuning space. The most common class of covariance kernel functions used is the Matérn class [61], which describes the similarity between two inputs and therefore between model outputs as well. One case of the Matérn class of functions

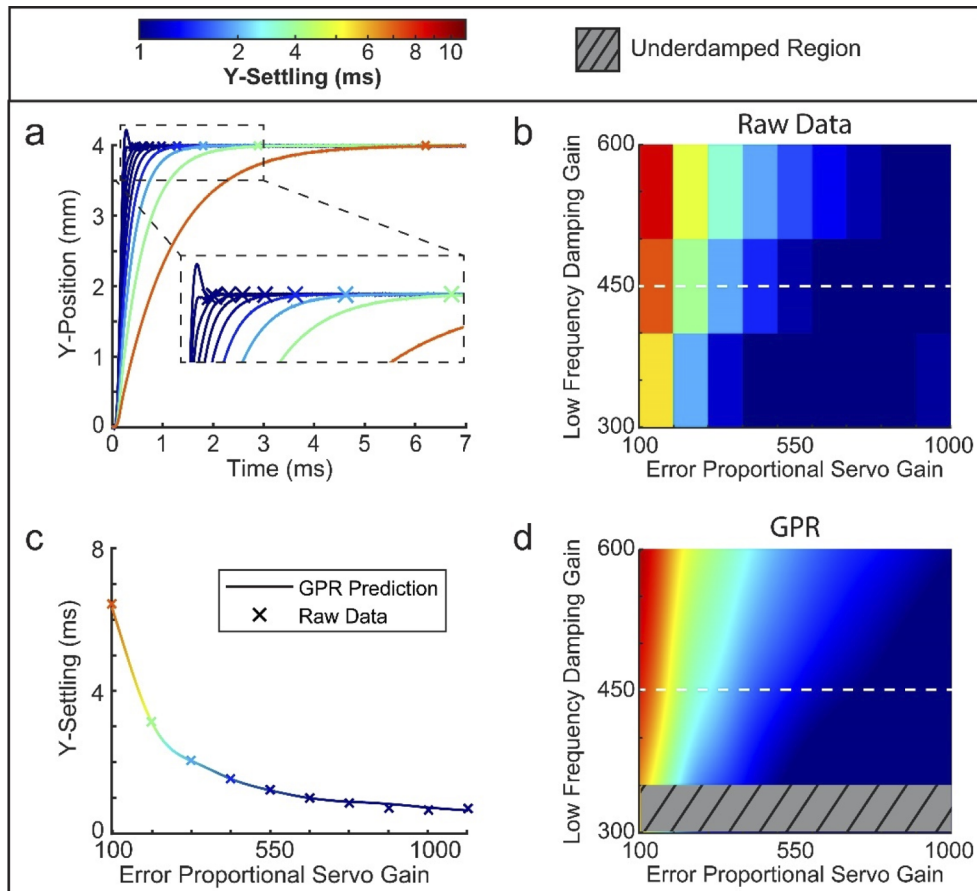


Fig. 3. Y-mirror settling time measurement and modeling example. (a) Raw position waveforms and corresponding settling times (cross) for increasing error proportional servo gain (right to left lines). (b) Heat-map aids visualization of settling time trends as a function of tuning parameters (dashed line corresponds to settling times in (a)). (c) Raw settling time data (cross) was used to generate a (d) 5-dimensional Gaussian process regression model used to predict global optimum tuning parameters.

is the squared exponential or Gaussian function:

$$k(x, x') = \sigma^2 \exp\left(-\frac{\|x - x'\|^2}{2l^2}\right) \quad (3)$$

In this case, σ^2 and l^2 are hyperparameters corresponding to the signal variance and length-scale, respectively. Gaussian processes with small signal variance produce values that stay close to the mean while those with large signal variance tend to deviate from the mean. Furthermore, Gaussian processes with a small length-scale tend to change rapidly while those with a large length-scale vary more slowly and are therefore smoother. By optimizing hyperparameter values, it is possible to generate a more robust prior distribution that better fits the signal trends of observed data, thus improving model accuracy.

The goal of GPR is to calculate a posterior probability distribution for predicting optimal settling time parameter values based on the initial prior settling time distribution and training observations. Given a set of settling time observations, $[x_t, S_t]$, the posterior probability distribution, $S' = P(S_0|S_t)$, can be calculated:

$$S' \sim \mathcal{N}\left(\overbrace{K(X_0, X_t)[K(X_t, X_t)]^{-1}S_t}^{\text{Posterior Mean}}, \underbrace{K(X_0, X_0) - K(X_0, X_t)[K(X_t, X_t)]^{-1}K(X_t, X_0)}_{\text{Posterior Covariance}}\right) \quad (4)$$

The posterior mean formula suggests that the prior settling time mean ($\mu_0 = 0$) is shifted to match the observed settling time values. Thus, inputs to the model that are closer to the observed parameter inputs will produce mean values closer to the observed settling time values. Similarly, the posterior covariance suggests that input parameters closer to the observed settling time inputs will have a lower variance.

GPR model training and optimization of the kernel function and corresponding hyperparameter values via 5-fold cross-validation was performed in MATLAB. Comparisons between optimal GPR performance and that of conventional regression methods, such as linear regression, decision tree regression, and support vector machine regression were also computed ([Supplement 1 Table 2](#)).

Galvanometer positional waveforms with underdamped step responses were excluded from the training data in order to improve the accuracy of the model for identifying optimal basic tuning parameters (Fig. 3(d)). GPR model predictions following the initial sweep showed optimal values of 0 for position error integral gain and position proportional gain (Fig. 4(a)), allowing for a reduction in dimensionality. A second parameter sweep was performed for the 3 remaining basic parameters (error proportional servo gain and low and high frequency damping gains) over a GPR predicted optimal range for each parameter with a step size of 50 (Fig. 4(b)-(d)). In addition, intermediate PID tuning parameters (low and high frequency damping filter cutoffs) were incremented from 5000-9000 Hz with a step size of 500 Hz for a total of 7,056 unique tuning configurations (N_2). Iterative parameter sweep and GPR model training was repeated until global optimum basic and intermediate PID tuning parameters were identified ([Supplement 1 Table 3](#)).

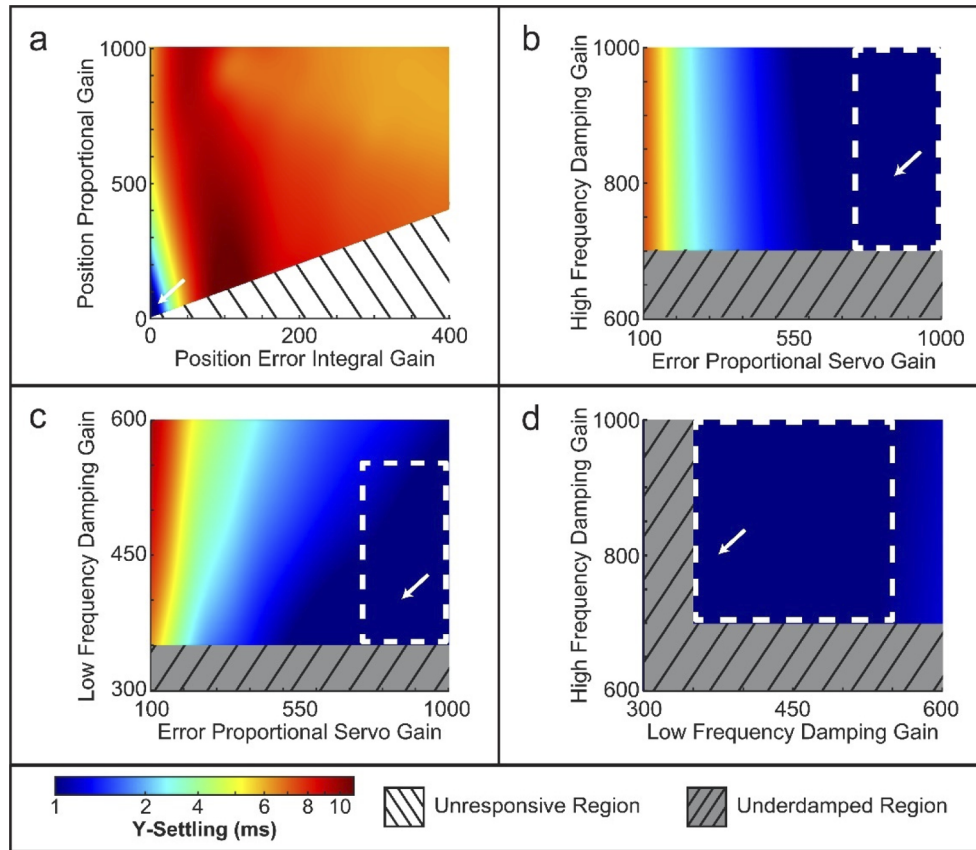


Fig. 4. Gaussian process regression predictions for the Y-mirror. (a) GPR model heat map of settling time as a function of position error integral gain and position proportional gain. Arrow shows minimum predicted settling time and optimal galvanometer step response when both parameters are 0. (b)-(d) Settling time heat maps for three remaining basic PID tuning parameters and position error integral gain and position proportional gain set equal to 0. Dashed white boxes show the predicted optimal range of values used to narrow the parameter search space in each dimension (arrow, minimum settling time).

3. Results

Galvanometer tuning optimization significantly reduced Y-mirror settling time as compared to default tunings for all measured input step amplitudes (Fig. 5, $p < 1E-10$). Specifically, the measured step responses show that settling time improves by 31-61% over manufacturer provided tunings for small input step amplitudes. For large step amplitudes, the optimized PID tuning improves settling time by 11-54%. Similarly, the optimized X-mirror tuning resulted in a 35-59% reduction in settling time as compared to the default tunings for a 4.5 mm (2.61 degree) step amplitude (Supplement 1 Fig. 3).

Motion during imaging integration time degrades lateral resolution by smearing the focal spot. Galvanometer response time plays a prominent role in this loss of resolution at FOV edges where scanning mirrors transition to and from high-speed return waveforms. Using measured galvanometer positions during these transitions, we computed the lateral motion between serial samples and effective lateral resolution normalized by the spot size compared against the Nyquist criterion conventionally used in point-scanning applications (Fig. 6). Expectedly, the optimized

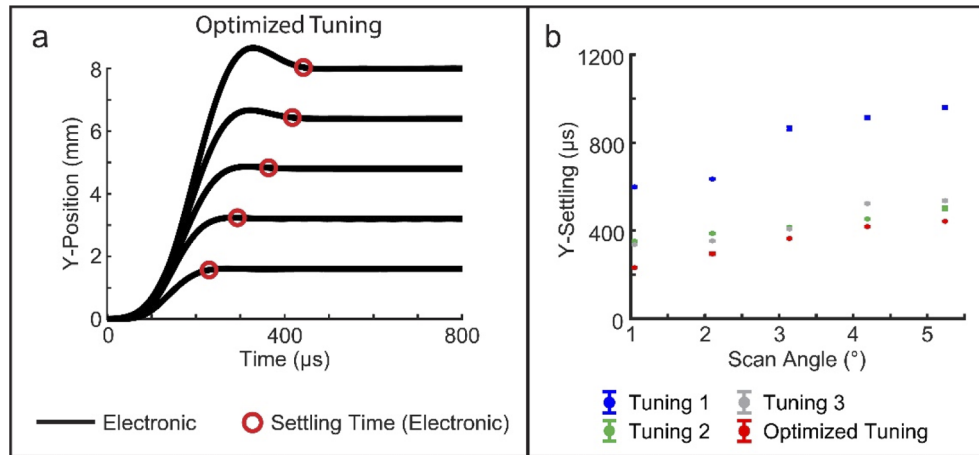


Fig. 5. Optimized tuning performance comparison. (a) Optimized tuning step responses and settling times for varying input step amplitudes. (b) Comparison between the settling times as a function of step angle measured for each PID tuning.

galvanometer had the highest resolution loss ($>4 \times$ FWHM), but also settles below the Nyquist sampling criterion 20-51% faster than those with default tunings. These results reiterate the advantage of optimized settling times and highlight the importance of quantitating galvanometer dynamics for point-scanning systems. Smeared and subsampled regions are routinely cropped and discarded, but galvanometer response dictates the amount of discarded data and, importantly, whether spatial resolution across the imaging FOV is uniform.

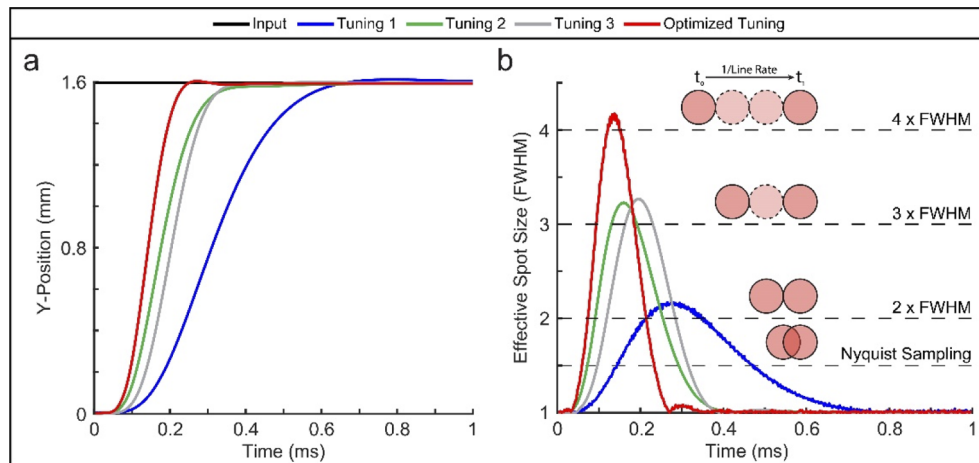


Fig. 6. Degradation of lateral resolution from galvanometer motion. (a) Galvanometer position waveform during a high-speed galvanometer positional reset. (b) Corresponding effective lateral resolution normalized by spot size FWHM.

The effect of optimized galvanometer response on point-scanning based imaging was validated using a fine distortion target (R1LS3P, ThorLabs) with a grid size of $10 \mu\text{m}$ and $50 \mu\text{m}$ spacing (Supplement 1 Fig. 4 and 5). In addition, we demonstrated the benefits for functional OCTA imaging (Supplement 1 Appendix A), 4D imaging of dynamic motion, and bi-directional scanning.

OCTA volumes were acquired in a healthy adult volunteer under an IRB-approved protocol using a handheld ophthalmic imaging probe. Sampling parameters were chosen to densely sample a small ROI below the central fovea of the retina (Table 1). Raster-scanning OCTA was performed using sampling protocol 1, which included a linear scan waveform (300 lines) and sinusoidal return waveform (500 lines) that set a fixed interscan delay of 2 ms between frames to visualize capillary flow. Linear scanning regions were identified as galvanometer positions with error deviations less than a spot size measured using corresponding PID controller positional readouts (Supplement 1 Fig. 6), and the corresponding OCTA images for each tuning (Fig. 7(b)) show that the optimized tuning has a 6-49% increase in linear FOV over the manufacturer provided tunings. In addition to FOV differences, the nonlinear scanning regions (Fig. 7(b), (d), (f), red) show feature deformations and degraded lateral resolution.

Table 1. Sampling protocols for OCTA imaging.

Sampling Protocol	Linear Scan Waveform (lines)	Return Waveform (lines)	Frames per Volume	Repeated Frames	Interscan Delay	Volume Acquisition Time
1	300	500	200	5	2 ms	2 s
2	800	0	200	5	2 ms	2 s
3	500	0	200	8	1.25 ms	2 s

We also evaluated the robustness of our galvanometer optimization to modified scan waveforms that benefit functional imaging by either increasing the linear FOV (Fig. 7(c) and (d)) or image SNR and contrast-to-noise (CNR) ratio (Fig. 7(e) and (f)). The following formulas were used to calculate CNR and SNR:

$$CNR = 20 * \log_{10} \left(\frac{\mu_{ROI}}{\sigma_{noise}} \right) \quad (5)$$

$$SNR = 20 * \log_{10} \left(\frac{I_{peak}}{\sigma_{noise}} \right) \quad (6)$$

Sampling protocol 2 increases the linear FOV by extending the linear scan waveform and removing the return waveform (Fig. 7(c)). The number of lines per frame and, thus, the interscan delay remain constant to maintain vascular flow velocity sensitivity. Sampling protocol 2 increases the linear FOV by 134-159% over sampling protocol 1 (Fig. 7(b) and (d)). Sampling protocol 2 effectively uses a sawtooth waveform, and since no return waveforms are explicitly sent to the PID controller, the length of the nonlinear galvanometer positional reset period is ultimately determined by its frequency response. Here, our optimized PID tuning increased the linear FOV by 12-55% over manufacturer provided tunings. As expected, by maintaining interscan delay, no significant differences in average image CNR or SNR were observed (Fig. 8(b) and (c)).

Optimized galvanometer response and modified scan waveforms can similarly be leveraged to improve image CNR and SNR. Sampling protocol 3 both extends the linear scan waveform and removes the return waveform from sampling protocol 1 to increase the linear FOV while reducing the interscan delay. Sampling protocol 3 increases the effective imaging frame rate such that the total number of repeated frames can be increased while maintaining total volume acquisition time (Fig. 7(e)). Again, there is a significant increase in linear FOV (30-49%, Fig. 7(b) and (f)) and mean SNR and CNR as a result of frame-averaging (8.8% and 6.7%, respectively, Fig. 8(b) and (c)) as compared to sampling protocol 1.

We demonstrate the benefits of optimized galvanometer response for 4D volumetric imaging of dynamic motion by comparing conventional (300 lines, 300 return lines, 100 frames) and optimized (370 lines, 0 return lines, 100 frames) sampling protocols over a 4×4 mm FOV (Fig. 9). Similar to OCTA protocols, return lines refer to a dedicated sinusoidal return waveform in the

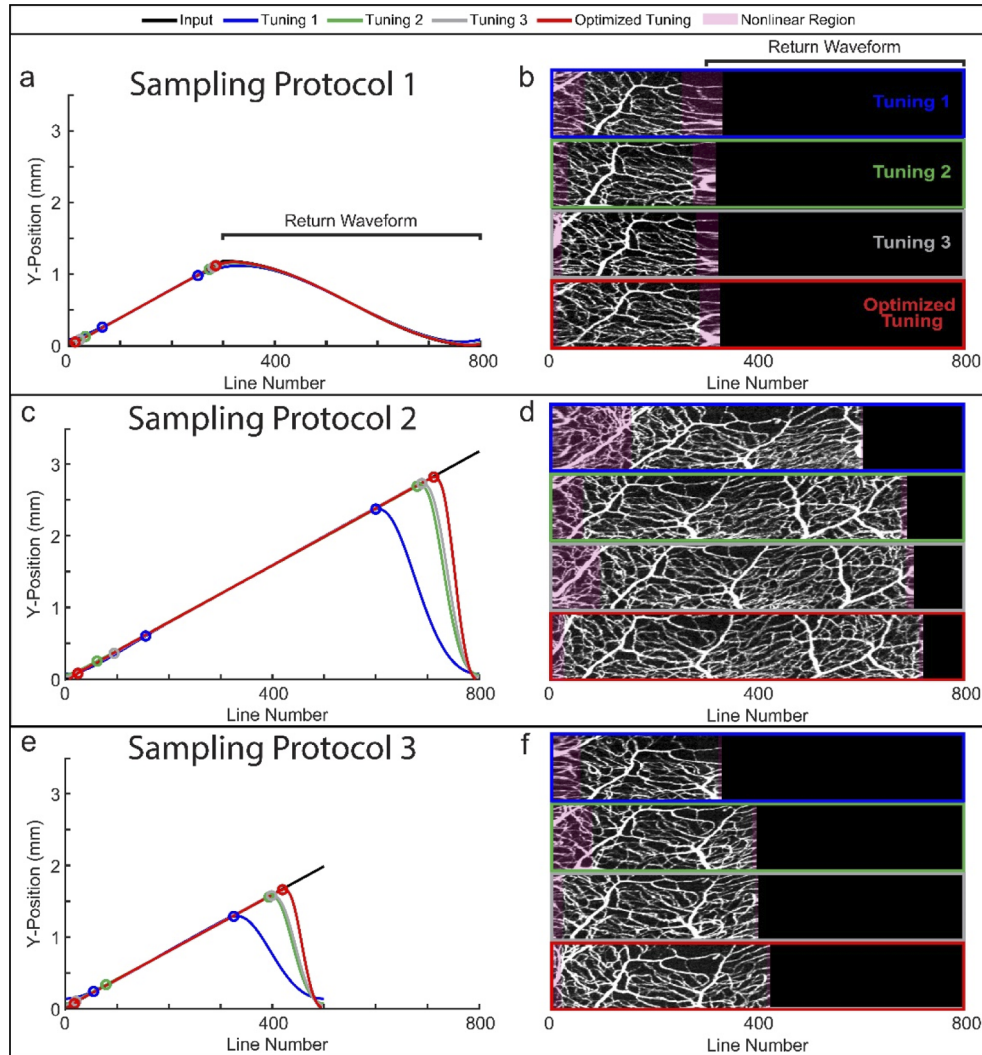


Fig. 7. OCTA acquisition protocol comparison. (a) Sampling Protocol 1 – Conventional OCTA scan waveform, measured position, and (b) corresponding *en face* OCTA projection for dense sampling of a small ROI. Regions of linear sampling are denoted by the colored circles. Nonlinear scan regions are highlighted in red on OCTA projections. (c) Sampling Protocol 2 – Modified scan waveform and (d) corresponding OCTA showing increased linear FOV by eliminating return lines between frames. (e) Sampling Protocol 3 – Modified scan waveform and (f) corresponding OCTA showing increase in linear FOV and decreased interscan delay.

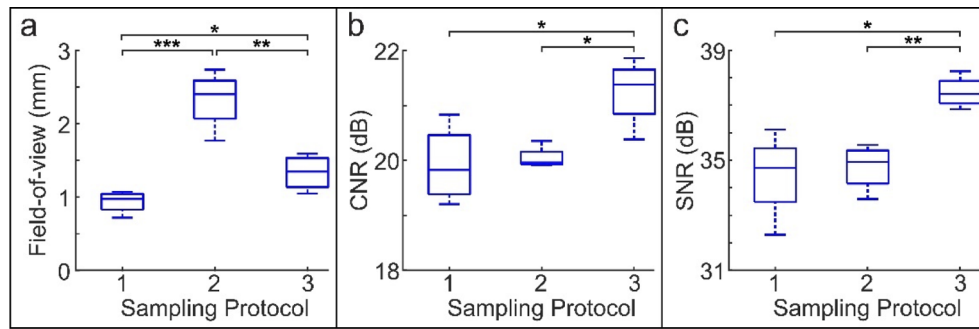


Fig. 8. Comparison between (a) linear FOV, (b) CNR, and (c) SNR between sampling protocols (* $p < 0.05$, ** $p < 0.01$, *** $p < 0.001$).

conventional protocol whereas the optimized protocol uses a sawtooth scan waveform without a dedicated return waveform and galvanometer positional reset occurs in the additional 70 lines of the scan (Fig. 7(c) and (e)). These return and reset regions were cropped, yielding identically

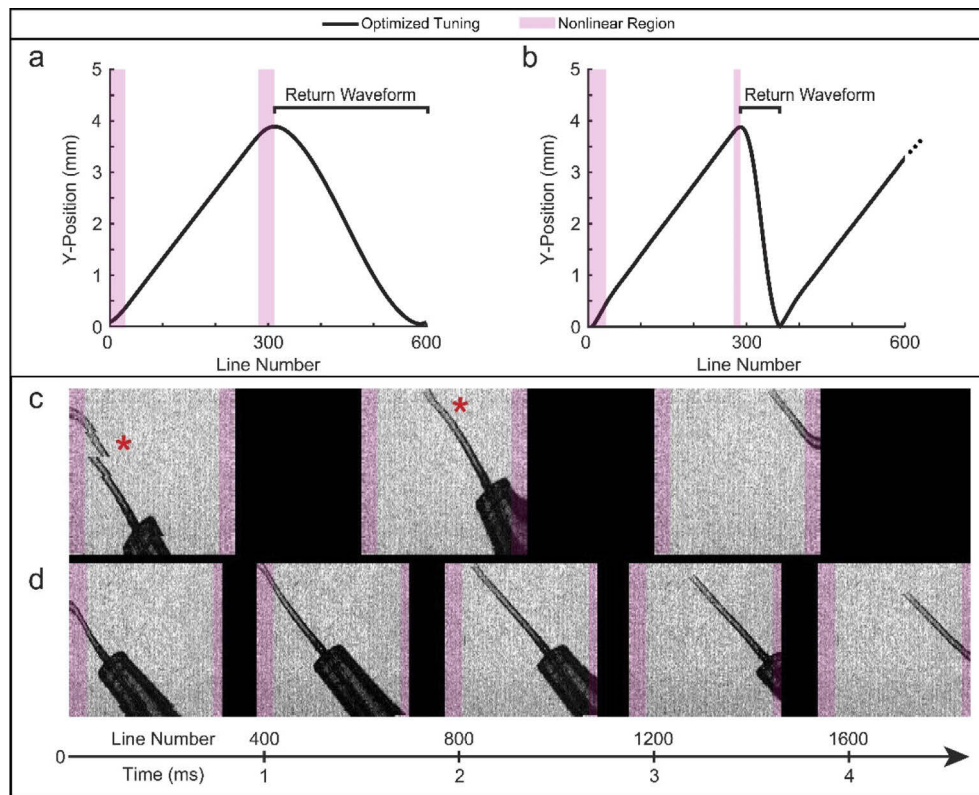


Fig. 9. 4D imaging of cannula dynamic motion using (a) conventional and (b) optimized sampling parameters. The series of acquired *en face* volume projections show (c) conventional sampling at lower volume rates (6.67 Hz) compared to (d) optimized sampling (10.81 Hz). Slower volume-rates result in discontinuities and distortion of the cannula tip (asterisk). Nonlinear scan regions are highlighted in red and show image distortions and degraded lateral resolution effects observed in Figs. 6 and 7.

sized and sampled volumes with $2560 \times 300 \times 100$ pix. (depth x lines x frames). Optimized sampling improves volumetric imaging speed by 62% over conventional sampling, enabling visualization of dynamic motion with fewer motion artifacts and distortions (Fig. 9(c) and (d); [Visualization 1](#) and [Visualization 2](#)).

Finally, we evaluated the benefits of optimized galvanometer response for bi-directional scanning, which can be used to effectively double scan speeds. Bi-directional galvanometer scanning can be limited by ringing at the sharp transition points, especially at higher scan speeds [50]. Here, the positional residual error with respect to the input waveform (Fig. 10) shows that our galvanometer optimization increases the linear FOV by 3-126% as compared to manufacturer provided PID tunings.

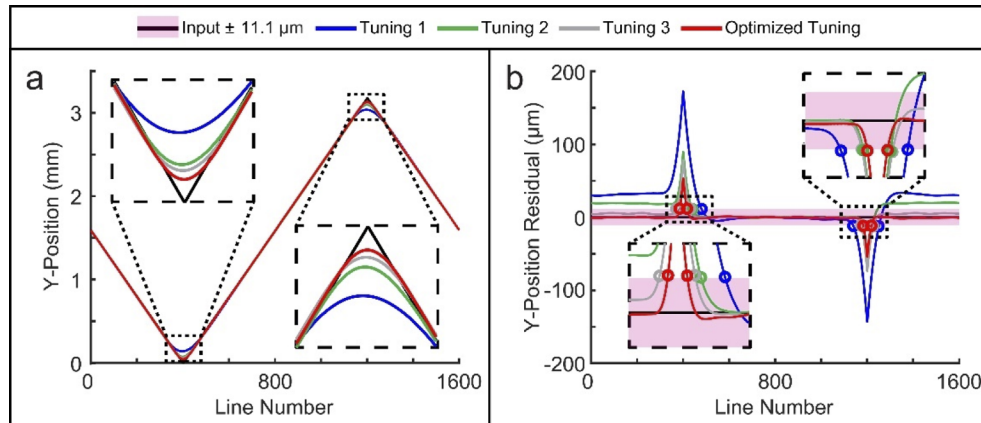


Fig. 10. Tuning comparison for bi-directional scanning. (a) Measured Y-mirror position waveforms from the galvanometer controller for an input bi-directional scan waveform and insets showing differences between tunings. (b) Position residuals used to calculate linear regions for each tuning within the lateral resolution error band. Start and stop positions for linear regions are shown by the corresponding colored circles.

4. Discussion and summary

Scanning technologies require robust high-speed performance. Galvanometer scanners are not constrained by fixed frequency, fixed FOV, or highly lossy/dispersive operation that limits resonant, polygon, and acousto-optic scanners. However, the performance of galvanometers is fundamentally limited by frequency response, which impacts settling time, sampling linearity, lateral resolution, and speed. By taking advantage of the closed-loop feedback unique to galvanometer controllers, it is possible to reduce the step response settling time by over 50% as compared to manufactured defaults. This reduction benefits applications requiring rapid scanning, such as 4D volumetric imaging, bi-directional scanning, and real-time tracking of ROIs.

The proposed hardware optimization also has significant advantages over previously reported methods, which are restricted to specific input waveforms. Here, we present methods of optimizing PID tuning parameters and the corresponding frequency response of the galvanometer controller, making the optimized tuning input-independent. As a result, it is possible to combine both hardware and software optimizations to further improve scanner performance and tailor scan waveforms specific to broad applications. Importantly, the method presented may be directly implemented without the use of specialized test equipment because we demonstrated that positional feedback from the galvanometer PID controller is sufficient for evaluating mirror response. As a proof-of-concept, we demonstrated hardware and software optimizations to increase linear FOV and image SNR/CNR in OCTA as well as to increase speed for rapid

volumetric imaging. However, similar advantages can be broadly achieved in point-scanning applications in imaging, display, ranging, manufacturing, and therapeutic technologies.

Funding. National Institutes of Health (R01-EY030490, R01-EY031769, T32-EB021937).

Acknowledgements. This research was supported by Vanderbilt University, the Vanderbilt Institute for Surgery and Engineering (VISE), and the US National Institutes of Health Grant No. R01-EY030490, R01-EY031769 and T32-EB021937. The content was solely the responsibility of the authors and does not necessarily represent the official views of the National Institutes of Health.

Disclosures. The authors declare no conflicts of interest.

Data Availability. All settling time and optimization data is available upon request.

Supplemental document. See [Supplement 1](#) for supporting content.

References

1. M. Minsky, "Memoir on inventing the confocal scanning microscope," *Scanning* **10**(4), 128–138 (1988).
2. W. Denk, J. H. Strickler, and W. W. Webb, "Two-photon laser scanning fluorescence microscopy," *Science* **248**(4951), 73–76 (1990).
3. A. H. Voie, D. H. Burns, and F. A. Spelman, "Orthogonal-plane fluorescence optical sectioning: Three-dimensional imaging of macroscopic biological specimens," *J. Microsc.* **170**(3), 229–236 (1993).
4. J. Huisken, J. Swoger, F. Del Bene, J. Wittbrodt, and E. H. K. Stelzer, "Optical sectioning deep inside live embryos by selective plane illumination microscopy," *Science* **305**(5686), 1007–1009 (2004).
5. J. Liang, D. R. Williams, and D. T. Miller, "Supernormal vision and high-resolution retinal imaging through adaptive optics," *J. Opt. Soc. Am. A* **14**(11), 2884 (1997).
6. A. Roorda, F. Romero-Borja, W. J. Donnelly III, H. Queener, T. J. Hebert, and M. C. W. Campbell, "Adaptive optics scanning laser ophthalmoscopy," *Opt. Express* **10**(9), 405 (2002).
7. R. H. Webb, G. W. Hughes, and F. C. Delori, "Confocal scanning laser ophthalmoscope," *Appl. Opt.* **26**(8), 1492 (1987).
8. M. W. Seeliger, S. C. Beck, N. Pereyra-Muñoz, S. Dangel, J. Y. Tsai, U. F. O. Luhmann, S. A. Van De Pavert, J. Wijnholds, M. Samardzija, A. Wenzel, E. Zrenner, K. Narfström, E. Fahl, N. Tanimoto, N. Acar, and F. Tonagel, "In vivo confocal imaging of the retina in animal models using scanning laser ophthalmoscopy," in *Vision Research* (Pergamon, 2005), **45**(28), pp. 3512–3519.
9. D. Huang, E. A. Swanson, C. P. Lin, J. S. Schuman, W. G. Stinson, W. Chang, M. R. Hee, T. Flotte, K. Gregory, C. A. Puliafito, J. G. Fujimoto, C. P. Lin, J. S. Schuman, and C. A. Puliafito, "Optical Coherence Tomography," *Science* **254**(5035), 1178–1181 (1991).
10. M. L. Stitch, E. J. Woodbury, and J. H. Morse, "Optical ranging system uses laser transmitter," *Electronics* **34**, 51–53 (1961).
11. N. J. Mankovich, A. M. Cheeseman, and N. G. Stoker, "The display of three-dimensional anatomy with stereolithographic models," *J Digit Imaging* **3**(3), 200–203 (1990).
12. R. Leyden, T. Almouist, M. Lewis, and H. Nguyen, "Stereolithography method and apparatus," (June 12, 1992).
13. Y. Bae, D. Soane, and C. Charles, "Rapid prototype three dimensional stereolithography," (May 27, 1993).
14. J. Allison, C. Childers, and C. Hull, "Method of making a three-dimensional object by stereolithography," (June 25, 1993).
15. G. Y. Fan, H. Fujisaki, A. Miyawaki, R. K. Tsay, R. Y. Tsien, and M. H. Ellisman, "Video-rate scanning two-photon excitation fluorescence microscopy and ratio imaging with cameleons," *Biophys. J.* **76**(5), 2412–2420 (1999).
16. H. Miyajima, N. Asaoka, T. Isokawa, M. Ogata, Y. Aoki, M. Imai, O. Fujimori, M. Katashiro, and K. Matsumoto, "A mems electromagnetic optical scanner for a commercial confocal laser scanning microscope," *J. Microelectromech. Syst.* **12**(3), 243–251 (2003).
17. A. D. L. Humphris, M. J. Miles, and J. K. Hobbs, "A mechanical microscope: High-speed atomic force microscopy," *Appl. Phys. Lett.* **86**(3), 1–3 (2005).
18. W. Wieser, W. Draxinger, T. Klein, S. Karpf, T. Pfeiffer, and R. Huber, "High definition live 3D-OCT in vivo: design and evaluation of a 4D OCT engine with 1 GVoxel/s," *Biomed. Opt. Express* **5**(9), 2963 (2014).
19. J. Huisken and D. Y. R. Stainier, "Even fluorescence excitation by multidirectional selective plane illumination microscopy (mSPIM)," *Opt. Lett.* **32**(17), 2608 (2007).
20. D. X. Hammer, R. D. Ferguson, C. E. Bigelow, N. V. Iftimia, T. E. Ustun, and S. A. Burns, "Adaptive optics scanning laser ophthalmoscope for stabilized retinal imaging," *Opt. Express* **14**(8), 3354 (2006).
21. A. Dubra and Y. Sulai, "Reflective afocal broadband adaptive optics scanning ophthalmoscope," *Biomed. Opt. Express* **2**(6), 1757 (2011).
22. Y. Geng, A. Dubra, L. Yin, W. H. Merigan, R. Sharma, R. T. Libby, and D. R. Williams, "Adaptive optics retinal imaging in the living mouse eye," *Biomed. Opt. Express* **3**(4), 715 (2012).
23. S. T. S. Holmström, U. Baran, and H. Urey, "MEMS laser scanners: A review," *J. Microelectromech. Syst.* **23**(2), 259–275 (2014).

24. H. Urey, "Torsional MEMS scanner design for high-resolution scanning display systems," in *Optical Scanning 2002*, S. F. Sagan, G. F. Marshall, and L. Beiser, eds. (SPIE, 2002), 4773(4), p. 27.
25. D. G. Tweed, "Resonant scanner linearization techniques," *Opt. Eng.* **24**(6), 241018 (1985).
26. J. Khoury, "Mapping approach for image correction and processing for bidirectional resonant scanners," *Opt. Eng.* **46**(2), 027007 (2007).
27. L. Xu, X. Tian, X. Li, G. Shang, and J. Yao, "Geometric distortion correction for sinusoidally scanned images," *Meas. Sci. Technol.* **22**(11), 114023 (2011).
28. Q. Yang, L. Yin, K. Nozato, J. Zhang, K. Saito, W. H. Merigan, D. R. Williams, and E. A. Rossi, "Calibration-free sinusoidal rectification and uniform retinal irradiance in scanning light ophthalmoscopy," *Opt. Lett.* **40**(1), 85 (2015).
29. M. Rajadhyaksha, R. R. Anderson, and R. H. Webb, "Video-rate confocal scanning laser microscope for imaging human tissues in vivo," *Appl. Opt.* **38**(10), 2105 (1999).
30. K. H. Kim, C. Buehler, and P. T. C. So, "High-speed, two-photon scanning microscope," *Appl. Opt.* **38**(28), 6004 (1999).
31. Y. X. Li, V. Gautam, A. Brüstle, I. A. Cockburn, V. R. Daria, C. Gillespie, K. Gaus, C. Alt, and W. M. Lee, "Flexible polygon-mirror based laser scanning microscope platform for multiphoton in-vivo imaging," *J. Biophotonics* **10**(11), 1526–1537 (2017).
32. V.-F. Duma and A. G. Podoleanu, "Polygon mirror scanners in biomedical imaging: a review," in *Optical Components and Materials X*, M. J. F. Digonnet, S. Jiang, and J. C. Dries, eds. (SPIE, 2013), 8621(11), p. 86210 V.
33. M. B. Bouchard, V. Voleti, C. S. Mendes, C. Lacefield, W. B. Grueber, R. S. Mann, R. M. Bruno, and E. M. C. Hillman, "Swept focally-aligned planar excitation (SCAPE) microscopy for high-speed volumetric imaging of behaving organisms," *Nat. Photonics* **9**(2), 113–119 (2015).
34. D. P. Biss, D. Sumorok, S. A. Burns, R. H. Webb, Y. Zhou, T. G. Bifano, D. Côté, I. Veilleux, P. Zamiri, and C. P. Lin, "In vivo fluorescent imaging of the mouse retina using adaptive optics," *Opt. Lett.* **32**(6), 659 (2007).
35. G. F. Marshall and G. E. Stutz, *Handbook of Optical and Laser Scanning* (CRC Press, 2018).
36. R. Salomé, Y. Kremer, S. Dieudonné, J. F. Léger, O. Krichevsky, C. Wyart, D. Chatenay, and L. Bourdieu, "Ultrafast random-access scanning in two-photon microscopy using acousto-optic deflectors," *J. Neurosci. Methods* **154**(1–2), 161–174 (2006).
37. T. Vettenburg, H. I. C. Dalgarno, J. Nylk, C. Coll-Lladó, D. E. K. Ferrier, T. Čižmár, F. J. Gunn-Moore, and K. Dholakia, "Light-sheet microscopy using an Airy beam," *Nat. Methods* **11**(5), 541–544 (2014).
38. M. Duocastella, G. Sancataldo, P. Saggau, P. Ramoino, P. Bianchini, and A. Diaspro, "Fast inertia-free volumetric light-sheet microscope," *ACS Photonics* **4**(7), 1797–1804 (2017).
39. G. R. B. E. Römer and P. Bechtold, "Electro-optic and acousto-optic laser beam scanners," *Physics Procedia* **56**(C), 29–39 (2014).
40. V. Iyer, B. E. Losavio, and P. Saggau, "Compensation of spatial and temporal dispersion for acousto-optic multiphoton laser-scanning microscopy," *J. Biomed. Opt.* **8**(3), 460 (2003).
41. T. Takamatsu and S. Fujita, "Microscopic tomography by laser scanning microscopy and its three-dimensional reconstruction," *J. Microsc.* **149**(3), 167–174 (1988).
42. R. H. Webb, "Confocal optical microscopy," *Rep. Prog. Phys.* **59**(3), 427–471 (1996).
43. J. Mertz, "Nonlinear microscopy: New techniques and applications," *Curr. Opin. Neurobiol.* **14**(5), 610–616 (2004).
44. W. Choi, C. Fang-Yen, K. Badizadegan, S. Oh, N. Lue, R. R. Dasari, and M. S. Feld, "Tomographic phase microscopy," *Nat. Methods* **4**(9), 717–719 (2007).
45. R. P. Aylward, "Advanced galvanometer-based optical scanner design," *Sens. Rev.* **23**(3), 216–222 (2003).
46. H. W. Yoo, S. Ito, and G. Schitter, "High speed laser scanning microscopy by iterative learning control of a galvanometer scanner," *Control Engineering Practice* **50**, 12–21 (2016).
47. A. Kasturi, V. Milanović, F. Hu, and H. J. Kim, "Iterative learning control (ILC) algorithm for greatly increased bandwidth and linearity of MEMS mirrors in LiDAR and related imaging applications," in *MOEMS and Miniaturized Systems XVII*, W. Piyawattanametha, Y.-H. Park, and H. Zappe, eds. (SPIE, 2018), **10545**, p. 37.
48. J. P. Giannini, A. G. York, and H. Shroff, "Anticipating, measuring, and minimizing MEMS mirror scan error to improve laser scanning microscopy's speed and accuracy," *PLoS One* **12**(10), e0185849 (2017).
49. V.-F. Duma, "Optimal scanning function of a galvanometer scanner for an increased duty cycle," *Opt. Eng.* **49**(10), 103001 (2010).
50. V. F. Duma, K. S. Lee, P. Meemon, and J. P. Rolland, "Experimental investigations of the scanning functions of galvanometer-based scanners with applications in OCT," *Appl. Opt.* **50**(29), 5735–5749 (2011).
51. V.-F. Duma, P. Tankam, J. Huang, J. Won, and J. P. Rolland, "Optimization of galvanometer scanning for optical coherence tomography," *Appl. Opt.* **54**(17), 5495 (2015).
52. J. G. Ziegler and N. B. Nichols, and others, "Optimum settings for automatic controllers," trans. ASME **64**(11), (1942).
53. C. Knospe, "PID control," *IEEE Control Syst.* **26**(1), 30–31 (2006).
54. Y. Li, K. H. Ang, and G. C. Y. Chong, "PID control system analysis and design: problems, remedies, and future directions," *IEEE Control Syst.* **26**(1), 32–41 (2006).
55. R. F. Spaide, J. G. Fujimoto, N. K. Waheed, S. R. Sadda, and G. Staurengi, "Optical coherence tomography angiography," *Progress in Retinal and Eye Research* **64**, 1–55 (2018).

56. M. T. El-Haddad, I. Bozic, and Y. K. Tao, "Spectrally encoded coherence tomography and reflectometry: Simultaneous en face and cross-sectional imaging at 2 gigapixels per second," *J. Biophotonics* **11**(4), e201700268 (2018).
57. J. D. Malone, M. T. El-Haddad, S. S. Yerramreddy, I. Oguz, and Y. K. K. Tao, "Handheld spectrally encoded coherence tomography and reflectometry for motion-corrected ophthalmic optical coherence tomography and optical coherence tomography angiography," *Neurophotonics* **6**(04), 1 (2019).
58. J. Jantzen and C. Jakobsen, "Turning PID controller tuning into a simple consideration of settling time," in *2016 European Control Conference, ECC 2016* (Institute of Electrical and Electronics Engineers Inc., 2017), pp. 370–375.
59. C. E. Rasmussen and C. K. I. Williams, *Gaussian Processes for Machine Learning* (n.d.).
60. E. Schulz, M. Speekenbrink, and A. Krause, "A tutorial on Gaussian process regression: Modelling, exploring, and exploiting functions," *Journal of Mathematical Psychology* **85**, 1–16 (2018).
61. N. Cressie and H. C. Huang, "Classes of nonseparable, spatio-temporal stationary covariance functions," *J. Am. Stat. Assoc.* **94**(448), 1330–1339 (1999).